Dispersion, Depletion, and Bridging of Athermal and Attractive Nanorods in Polymer Melt

2 AUTHORS:

Uma Sankar
Saudi Basic Industries Corporation (SABIC)

1 PUBLICATION   **0** CITATIONS

SEE PROFILE

Mukta Tripathy
Indian Institute of Technology Bombay

8 PUBLICATIONS   **328** CITATIONS

SEE PROFILE

Dispersion, Depletion, and Bridging of Athermal and Attractive Nanorods in Polymer Melt

Uma K. Sankar and Mukta Tripathy*

Department of Chemical and Engineering, Indian Institute of Technology Bombay, Powai, Mumbai 400076, India

Ⓢ Supporting Information

ABSTRACT: We report a detailed theoretical study of polymer nanorod composites using integral equation theory. The miscibility criteria for small amounts of nanorods in a dense polymer melt have been predicted for various polymer adsorption strengths, nanorod thicknesses, smoothnesses, and aspect ratios, for both athermally interacting and attractive rods. Close comparisons with the nanosphere limit have been made. We find that nanorods exhibit the same kinds of depletion, dispersion, bridging, and telebridging behavior previously predicted for spherical particles. However, the limits of these behaviors are a close (and sometimes nonmonotonic) function of aspect ratio, surface roughness, and nanorod thickness. The miscible region between depletion-driven phase separation and bridging driven phase separation quickly narrows with increasing aspect ratio and remains roughly constant as the nanorod radius of gyration exceeds that of the polymer. This miscible window narrows more quickly in the case of attractive rods. The polymer-mediated attractive forces between athermal rods scale with nanorod diameter, in both the bridging and depletion regimes. Telebridged structures are predicted when the range of polymer–particle attractions approaches the polymer thickness, i.e., the monomer diameter.
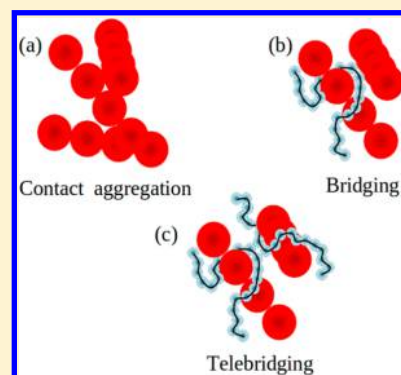
I. INTRODUCTION

Carbon black reinforced rubber tires have seen a century of use. However, it has only been in the last few decades that a large volume of research on the topic of polymer nanocomposites has been conducted. The advantages of nanoparticle-filled polymer composites over pure polymer melts in terms of improved mechanical, thermal, optical and rheological properties are, now, well-known by materials scientists.[1–3] Apart from these property improvements, polymer nanocomposites have specialized applications in fuel cells,[4,5] liquid sensing,[6,7] bone repair,[8,9] and targeted drug delivery.[10] Advances in the past decade have brought forth important applications of nanorod/nanotube filled polymers such as highly conducting carbon nanotube[11] and metal nanowire composites,[12] optically active gold nanorod composites,[13] and light harvesting semiconductor nanorod composites.[14] However, due to entropic depletion-driven phase separation,[15–18] solubilizing the nanoparticles in a polymer melt continues to remain a problem. Moreover, introducing carbon nanotubes in a polymer melt presents an additional challenge. While dispersing a small amount of carbon nanotubes in a polymer matrix gives rise to strong mechanical reinforcement,[19] high thermal and electrical conductivity,[11,20] and fire retardancy,[21] the strong van der Waals interactions (in addition to the depletion-induced "effective attractions") render them difficult to disperse. Hence, in cases where carbon nanotubes are found to be dispersed well in composites, it is usually because they are kinetically stabilized.[22,23]

While depletion-induced attractions affect phase separation between noninteracting polymer–particle mixtures,[24] introducing attractive interactions between polymers and nanoparticles

causes nanoparticles to be well-dispersed in the polymer melt.[25] When these attractive interactions become large, both theory[26–29] and simulations[30–35] predict a "bridging"-induced phase separation. In the latter state, nanoparticles are "bridged" together through their common attraction to polymers. There is therefore, a window of miscibility where an adsorbing polymer can be used to form a well dispersed nanocomposite. Mixtures of rods and nonadsorbing polymers have been studied using free volume theory[36] and Monte Carlo simulations,[37] and they report depletion-induced phase separation in the melt limit. Simulations,[38] mean field theory,[39] and self-consistent Polymer Reference Interaction Site Model (PRISM) theory[40] have been used to study the polymer dimensions close to the nanoparticle surface. While most of these studies have been conducted for spherical nanoparticles, recent work involving self-consistent field theory,[41–43] PRISM theory,[44] molecular dynamics,[32,38] and Monte Carlo[45] simulations have probed the behavior of aspherical particles (including nanorods, and nanotubes) in polymer melts and films.

High aspect ratio conducting nanoparticles such as carbon nanotubes, metal nanorods and nanowires can be dispersed in a nonconducting polymer melt to form a percolated, system-spanning network that provides pathways for charge carriers to travel, creating tough conducting materials. At the electrical percolation threshold, these materials exhibit a sudden, several orders of magnitude, rise in conductivity.[12] Certain materials

allow electron tunneling and therefore can have slightly lower percolation thresholds. On the other hand the "rheological percolation threshold" is somewhat less well-defined. It is usually described by the appearance of a plateau in the elastic modulus (G') at low frequencies,[46−49] indicating a crossover to a more solid-like response to shear. However, studies differ on whether the rheological percolation threshold appears before (at lower volume fraction) or after (at higher volume fraction than) the electrical percolation threshold. This usually depends on the materials used, degree of alignment of rods, processing method, and temperature. The morphological requirements for rheological percolation are still a matter of debate.[46,48] In recent years, two kinds of rheological percolation thresholds (the "soft rheological threshold", and "rigid rheological threshold") have been discussed.[48] The electrical percolation threshold is consistent with the geometric idea of connectedness through inter-rod contacts, and hence more amenable to theories which predict structure and morphology. Nanorod percolation thresholds of pure rods have been determined using integral equation theories,[50−54] modified Bethe lattice approaches,[54,55] the random contact model,[56,57] and Monte Carlo simulations.[58,59] These studies find that the percolation thresholds of monodisperse,[58] polydisperse,[54,55,57,59] and flexible[51] nanorods decrease with rod aspect ratio in a power-law fashion. Self-consistent field theory study by Surve et al.[41] and integral equation theory by Wang et al.[60] have explicitly included the effect of polymers on the percolation of nanorods.

In this article we use PRISM theory to predict the structure, and phase behavior of adsorbing polymer-nanorod composites at various adsorption strengths, nanorod interactions, rod thicknesses and rod aspect ratios. PRISM theory has been used to study polymer nanocomposites, and its results have provided qualitatively accurate comparisons against experiments[61,62] and simulations.[26,30,31] However, PRISM results are sensitive to the kinds of closures invoked,[26] and it is difficult to determine *a priori* the most suitable closure for a given problem. We have chosen closures established by previous researchers[26] and also tested against results of dissipative particle dynamics simulations.[63] We perform a detailed investigation into the effect of nanorod geometry, and rod interactions in dispersion, depletion, and bridging of nanorods within the matrix polymer at very small rod density. Section II details the model used for polymers and nanorods, as well as the methodology adopted to determine the phase boundaries. In section IIIA, we present the microscopic structure of the nanocomposite through two-particle correlations, while section IIIB discusses the effect of rod geometry on the phase diagrams of the nanocomposites, and the forces between nanorods. Section IIIC comments on the structure and phase behavior of attractive rods. Finally, section IV gives a short summary and conclusions.

II. MODEL, THEORY, AND METHODOLOGY

We employ the integral equation PRISM theory by using a spherical site-level description of both polymers and rods. Polymers are modeled as a flexible chain of $N_p = 100$ spherical sites with diameter $d = 0.5$, and the distance between adjacent monomers is denoted by l (we have taken $l/d = 1.33$). The rods are modeled as N_n rigidly arranged spherical sites of diameter D, that are placed linearly and tangentially. The distance between the spherical sites on the rod is denoted by L, and we have chosen $L/D = 1$ for most of this study. The aspect ratio (AR) of the rod, is therefore equal to the number of spherical sites on the rod, and a rod with $N_n = $ AR $= 1$ is simply a sphere.

In this study, we have studied rods with diameters, $D = 0.5, 1, 2,$ and 5, such that $D/d = 1, 2, 4, 10$ and aspect ratios varying in the range AR $= 1−100$. The polymer nanocomposite has a total volume fraction of $\eta_t = 0.4$, and of this the fraction of nanoparticle is $\varphi_n = 0.01$ making the volume fraction of nanoparticles $\eta_n = 0.004$.

PRISM theory uses the generalization of the Ornstein−Zernike equation for spherical particle fluids to aspherical particles that was first introduced by Chandler et al.,[64] and then invokes an equivalent-site approximation[65−67] that treats all chemically similar sites within a given (molecular) species equivalently. The latter is done in order to make the coupled integral equations solvable for large molecules, and has the consequence of averaging correlations over all sites of a given species (polymer or nanorod). The problem is then posed in terms of correlations between two types of sites−polymer sites (p) and nanoparticle sites (n). This approximation results in reducing a $(N_p + N_n)/2 \times (N_p + N_n)/2$ matrix equation to a 2×2 matrix equation. The matrix form of the coupled integral equations in Fourier space is written as follows.

$$\underline{H}(k) = \underline{\Omega}(k)\underline{C}(k)[\underline{\Omega}(k) + \underline{H}(k)] \tag{1}$$

Here $\underline{H}(k)$, $\underline{\Omega}(k)$ and $\underline{C}(k)$ are the matrices of density scaled pair correlation functions ($H_{ij}(k) = \rho_i\rho_j h_{ij}(k)$), density scaled intramolecular distributions, and the direct correlation functions respectively between sites of type i and j where ρ_i is the number density of spherical sites of type i. The pair correlation function is related to the radial distribution function by $g_{ij}(r) = 1 + h_{ij}(r)$. For chemically homogeneous polymers and rods within the equivalent site approximation, $\underline{\Omega}(k)$ is a diagonal matrix with elements $\underline{\Omega}_{ij}(k) = (\rho_i\rho_j)^{1/2}\omega_{ij}(k)\delta_{ij}$. Equation 1 is solved iteratively in conjunction with the Percus−Yevick (P−Y) closure for polymer−polymer and polymer−nanoparticle interactions, and the hypernetted chain (HNC) closure equation for nanoparticle−nanoparticle correlations. The P−Y and HNC closures are given, respectively, by eqs 2 and 3, where $U_{ij}(r)$ is the interparticle potential between sites of type i and j, and $\beta = k_BT$.

$$C_{ij}(r) = (1 - e^{\beta U_{ij}(r)})(1 + h_{ij}(r)) \tag{2}$$

$$C_{ij}(r) = h_{ij}(r) - \beta U_{ij}(r) - \ln(1 + h_{ij}(r)) \tag{3}$$

As mentioned earlier, PRISM results are sensitive to the kind of closure approximations used. We have also studied the same system using the HNC closure for the polymer−particle interactions, and have found disagreements with simulation results[63] (as will be discussed later). Hence, the results that we present here have been reached using the P−Y closure for polymer−particle interactions. While the polymer−polymer interactions are of a purely hard core nature, polymer−particle and particle−particle interactions are modeled by a hard core followed by an exponentially decaying attraction of the following form.

$$U_{ij}(r) = \infty, \qquad r \leq \sigma_{ij}$$

$$U_{ij}(r) = -\varepsilon_{ij}e^{-(r-\sigma_{ij})/\alpha_{ij}}, \quad r \leq \sigma_{ij} \tag{4}$$

In eq 4, $\sigma_{pn} = (D + d)/2$, $\sigma_{nn} = D$, ε_{pn} is the polymer−particle attraction strength, ε_{nn} is the particle−particle attraction strength, $\alpha_{pn} = 0.133(D + d)/2$, is the range of attraction between polymer and nanoparticle sites, and $\alpha_{nn} = 0.1D$ is the range of attraction between nanoparticle sites. This form of the

polymer−particle potential is chosen since it mimics the van der Waals interaction between colloidal particles.[27,68] (Henderson et.al.[68] have derived an expression for an integrated Lennard-Jones potential between two colloid-sized particles. Later Hooper et al.[27] have shown that the attractive portion of the potential is not unlike an exponentially decaying attraction.) In this study, $\varepsilon_{nn} \geq 0$ (nanoparticles either interact athermally or are attractive) while ε_{pn} is sometimes negative. The latter is used to determine the miscibility limits of short diameter nanospheres in polymer (as will be discussed in section IIIB). We present the miscibility conditions as a phase diagram in the ε_{pn}/k_BT—aspect ratio plane at several $\varepsilon_{nn}/|\varepsilon_{pn}|$. From here forward we will denote $\varepsilon_{nn}/|\varepsilon_{pn}|$ as $\varepsilon_{nn}/\varepsilon_{pn}$. The polymer intramolecular distribution function as given by the freely jointed chain (FJC) model[67] is written as,

$$\omega_{pp}(k) = [1 - f^2 - 2N_p^{-1}f + 2N_p^{-1}f^{N_p+1}]/(1-f)^2 \tag{5}$$

where $f = \sin(kl)/kl$ and l is the rigid bond length between two adjacent monomers. The radius of gyration of the FJC polymer is $Rg_{poly} = l(N_p/6)^{1/2} = 5.43d$). The intramolecular distribution function for rigid rods in real space is given by a summation of Dirac delta functions.

$$\omega_{nn}(r) = \frac{1}{N_n} \sum_{\nu,\gamma}^{N_n} \delta(r - |\vec{r}_{\nu\gamma}|) \tag{6}$$

Here, $\vec{r}_{\nu\gamma}$ is the vector distance between sites ν and γ on the same rod. In Fourier space, the intramolecular distribution function is written as,

$$\omega_{nn}(k) = \frac{1}{N_n}\left[N_n + 2 \sum_{\lambda=1}^{N_n-1} (N_n - \lambda)\frac{\sin \lambda kL}{\lambda kL} \right] \tag{7}$$

where, L is the distance between adjacent sites on the rod. Using the solutions to the PRISM equation, the matrix of density scaled static structure factors can be obtained from the expression,

$$\underline{S}'(k) = [\underline{I} - \underline{\Omega}(k)\,\underline{C}(k)]^{-1}\underline{\Omega}(k) \tag{8}$$

The structure factors are calculated by the relationship, $S_{ij}(k) = S'_{ij}(k)/(\rho_i\rho_j)^{1/2}$.

The static structure factor, $S(k)$, is a measure of concentration fluctuations, and its divergence at $k = 0$ is indicative of spinodal macrophase separation. We solve the PRISM integral equations for a given composition while incrementing ε_{pn}, to determine the limits of convergence of the coupled equations. The inset of Figure 1 plots the nanoparticle−nanoparticle collective structure factor at $k = 0$ for nanorods of AR = 10. It illustrates a rapid rise in $S_{nn}(k = 0)$, as the limit of convergence (in terms of ε_{pn}) is approached. As has been reported previously,[44,69] we find that the convergence limits correspond closely with the value of ε_{pn} at which $1/S_{nn}(0)$ would extrapolate to zero. We, therefore, take the last converged value of ε_{pn} (accurate up to four decimal places) to be the spinodal boundary. Although the inset of Figure 1 shows a sharp, nearly vertical, rise in $S_{nn}(0)$ as the phase boundary is approached, the range of values is not very large. This is due to the low concentration of nanoparticles in the composite. In this limit, $S_{nn}(k) = \omega_{nn}(k) + \rho_n h_{nn}(k) \rightarrow \omega_{nn}(k)$ and $\omega_{nn}(k = 0) = N_n$. Hence the $S_{nn}(0)$ values that are plotted in the inset of Figure 1 are close to $N_n = 10$. We, therefore, also
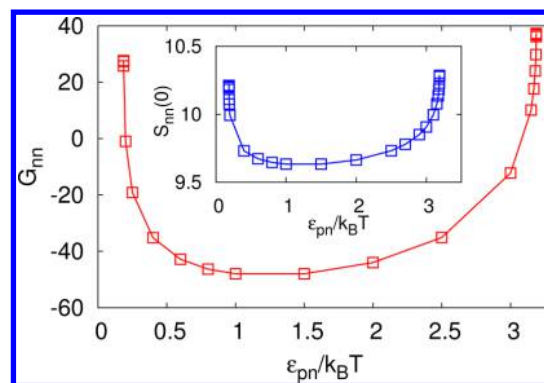
Figure 1. Main panel: Kirkwood Buff integral values, G_{nn}. Inset: particle−particle collective structure factors at zero wave vector, $S_{nn}(k = 0)$, as a function of polymer−particle interaction strength ε_{pn}/k_BT for rods with AR = 10 and $D/d = 2$.

plot the Kirkwood−Buff integral given by eq 9 in the main panel of Figure 1.

$$G_{nn} = 4\pi \int_0^\infty (g_{nn}(r) - 1)r^2 \, dr = h_{nn}(k = 0) \tag{9}$$

The figure shows a rapid rise in the Kirkwood-Buff integrals as the convergence limits are reached, which indicates macrophase separation. We have also calculated the orientationally averaged forces between rod sites through the following expression, where $W_{nn}(r)$ is the potential of mean force between two nanoparticle sites.

$$f_{nn} = -\frac{dW_{nn}(r)}{dr} = \frac{d\{\ln[g_{nn}(r)]\}}{dr} \tag{10}$$

Since PRISM treats all the sites of a rod in an averaged manner, it does not appropriately capture the alignment of rods. Rod alignment becomes likely in the presence of attractions (solvent-induced or direct). The microscopic structure data that we present, is spherical site-averaged, and does not take into account, inter-rod angular correlations. However, at the low rod volume fractions that we are considering here ($\eta_n = 0.004$), we do not think it likely that rod alignment would affect the phase behavior of the nanocomposites.

III. RESULTS

A. Microscopic Structure of Athermal Rods.
Entropic depletion causes polymer and nanoparticles to phase separate.[16,24] Inducing moderate attractions between polymers and nanospheres, results in a miscible composite. However, at very large adsorption strengths, particles are bridged by their common attraction to polymers, and a bridging-induced phase separation is observed.[25,27,31,32] We predict a similar kind of behavior in the case of athermal and attractive nanorods. Figure 2a shows the nanoparticle−nanoparticle radial distribution function, $g_{nn}(r)$, of athermal spheres with $D/d = 4$, while Figure 2b presents $g_{nn}(r)$ of athermal rods with AR = 10 and $D/d = 4$ within the site-level description. At low attractions between the polymer and nanoparticle (ε_{pn}), the radial distribution function displays very large contact peaks (at particle volume fraction of $\eta_n = 0.004$), indicating a high degree of clustering. As the adsorption strength of the polymer rises, the contact peak reduces drastically, and a well-dispersed mixture is obtained. At large adsorption strengths our calculations predict low contact
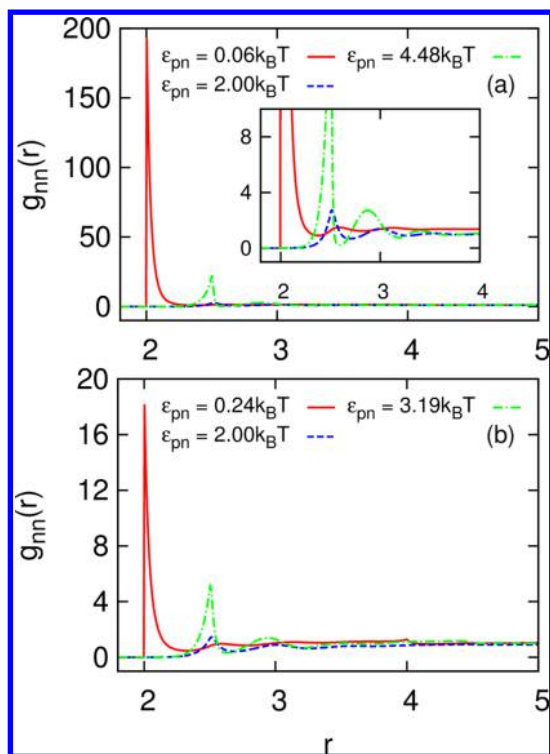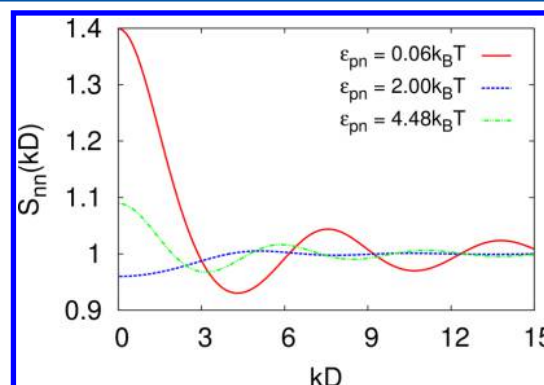
Figure 2. Particle−particle radial distribution function for $D/d = 4$ particles (a) spheres, at $\varepsilon_{pn} = 0.06 k_B T$ (solid, red line), $\varepsilon_{pn} = 2k_B T$ (dashed, blue line), and $\varepsilon_{pn} = 4.48 k_B T$ (dot-dashed, green line) and (b) rods with AR = 10, at $\varepsilon_{pn} = 0.24 k_B T$ (solid, red line), $\varepsilon_{pn} = 2k_B T$ (dashed, blue line), and $\varepsilon_{pn} = 3.19 k_B T$ (dot-dashed, green line).

between nanoparticles due to their preferential interaction with polymers. However, unusually large peaks are observed at $r = D + d$. These peaks correspond to polymer-bridged correlations between nanoparticles. A single monomer binds to two nanoparticles which results in the bridging peak at $g_{nn}(D + d)$. Figure 3b illustrates the bridged arrangement of two nanorods by means of their attractive interaction with the intervening polymer, while Figure 3a depicts depletion-driven contact aggregation of the nanorods at low ε_{pn}. Parts a and b of Figure 2 indicate that the depletion-to-dispersion-to-bridging
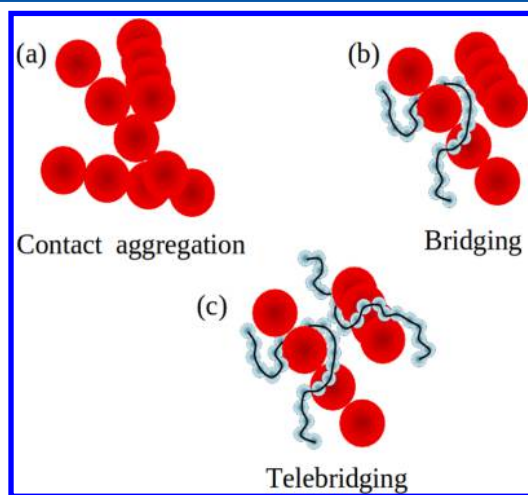
Figure 3. Schematic of different types of morphologies obtained for nanoparticle aggregation in a polymer matrix. (a) Contact aggregation, (b) bridging aggregation, and (c) telebridging.

transition is common to nanospheres and nanorods. However, the size of the contact and bridging peaks fall significantly for nanorods. As the aspect ratio increases from 1 (for spheres), interparticle correlations between nanoparticle sites are sterically hindered due to the presence of attached sites (intraparticle correlations), and this results in lower contact, $g_{nn}(D)$, and bridging, $g_{nn}(D+d)$ peaks. The peaks fall drastically between aspect ratios of 1 and 6, and then change rather slowly. The latter is due to the fact that site-level steric hindrance is a local interaction, and the interparticle contact (and bridging) correlations are unaffected by the presence of sites many rod-diameters away. Figure 4 presents the static structure factor of

Figure 4. Particle−particle collective static structure factor for $D/d = 4$ spheres, at $\varepsilon_{pn} = 0.06 k_B T$ (solid, red line), $\varepsilon_{pn} = 2k_B T$ (dashed, blue line), and $\varepsilon_{pn} = 4.48 k_B T$ (dot-dashed green line).

nanospheres, $S_{nn}(kD)$, within the polymer melt. Large zero wavevector values at very low and very high ε_{pn} indicate a tendency toward macroscopic phase separation, corresponding to depletion-driven, and bridging-driven phase separation, respectively. In the depletion (low ε_{pn}) regime, the largest peak (besides at $k = 0$) appears at $k \sim 2\pi/D$, indicating liquid-like ordering on the particle length scale. However, at high ε_{pn}, the largest nonzero wavevector peak indicates liquid ordering at $k \sim 2\pi/(D+d)$. The latter indicates repeating bridged structures within the phase separating polymer−nanoparticle mixture. This small bridging peak disappears for nanorods, as the bridging correlations in the radial distribution function are diminished.

PRISM calculations of polymer−sphere composites[27] (in the dilute sphere limit), have predicted microstructures where two spherical particles are bridged by multiple polymer layers, as the range of the polymer particle attraction increases. This phenomenon has been called "telebridging". Molecular dynamics simulations have pointed to the existence of telebridging between spherical particles at high attraction strengths.[70] However, it is unclear whether such telebridging is a result of long polymer desorption times. Figure 5 illustrates the nanoparticle−nanoparticle radial distribution as a function of the interparticle distance subtracted by the particle diameter, for polymer−nanorod (AR = 25) composites at four different rod diameters. The radial distribution functions are chosen for mixtures close to bridging-driven phase separation. The figure shows that for $D/d = 1$, 2, and 4, the contact values diminish, and the bridging peak grows with increasing particle diameter. Moreover, it demonstrates that while for $D/d = 1, 2,$ and 4, the largest peak in $g_{nn}(r − D)$ appears at a single monomer diameter away from contact (this being the bridging peak at $r − D = d$), for $D/d = 10$, the largest peak appears three polymer
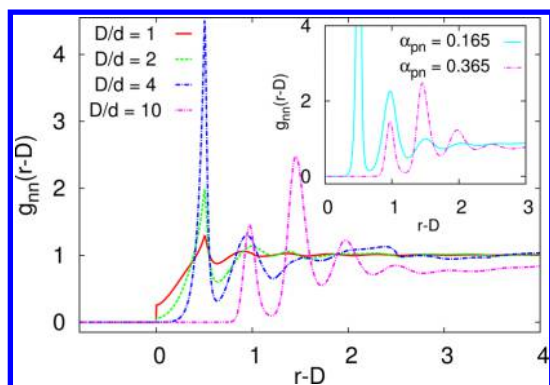
Figure 5. Particle−particle radial distribution function in the bridging regime for athermal nanorods with AR = 10, D/d = 1 (solid, red line), D/d = 2 (dashed, green line), D/d = 4 (dot-dashed blue line), and D/d = 10 (dot-dot-dashed pink line). Inset shows $g_{nn}(r)$ for AR = 10, D/d = 10 rods with α_{pn} = 0.165 (solid, light blue line) and α_{pn} = 0.365 (dot-dot-dashed pink line).

diameters away ($r − D = 3d$). Hence, while the smaller diameter nanorods are bridged by a single polymer layer, at D/d = 10 the nanorods are bridged by two to four polymer layers (as evidenced by prominent peaks two, three, and four polymer diameters away from $r = D$). The radial distribution function at D/d = 10 represents telebridged structures, such as those depicted by Figure 3c. However, this transition from bridging to telebridging is not a function of particle diameter, rather a function of the polymer−particle attractive range (α_{pn}). Since the range of the exponentially decaying attraction scales with particle size (α_{pn} = 0.133$(D + d)/2$), at D/d = 10, the attractive

range becomes larger than the monomer radius (α_{pn} = 0.365 > 0.25). This enables several adsorbed polymer layers to experience attractions with the two nanoparticles that they bridge. We have calculated the radial distribution functions of D/d = 10 rods with smaller polymer−particle attraction range (α_{pn} = 0.165) and of D/d = 4 rods at larger α_{pn} = 0.365. We find that while the former switches over to bridging behavior (inset of Figure 5) as the attractive range decreases, the latter shifts toward telebridging as the α_{pn} increases (data not shown). Similar behavior is predicted for all particle aspect ratios (including AR = 1 spheres). We, therefore, surmise that it is the range of the polymer−nanoparticle attraction, rather than the strength of the attraction, or the diameter of the nanoparticle that controls telebridging.

B. Phase Behavior of Athermal Rods. While qualitatively, nanorods display similar kinds of microstructures, as well as phase behavior to that of nanospheres in polymer melt, the key difference is in the location of the phase boundary and the width of the miscible region. The latter is of immense engineering importance. The spinodal phase diagrams of polymer-nanorod composites as a function of polymer−nanoparticle attraction strength, rod aspect ratio, particle size, and rod−rod attraction strengths are given by Figure 6. These phase diagrams are constructed using the $S_{nn}(k = 0)$ criteria discussed in Section II. For all four particle diameters, D/d = 1, 2, 4, and 10, presented in Figure 6a−d, respectively, the miscibility window that lies between depletion-driven phase separation at low ε_{pn}, and bridging-driven phase separation at high ε_{pn} narrows with increasing aspect ratio. The rise in the depletion-driven phase separation boundary has also been predicted by dissipative particle dynamics simulations.[63] We
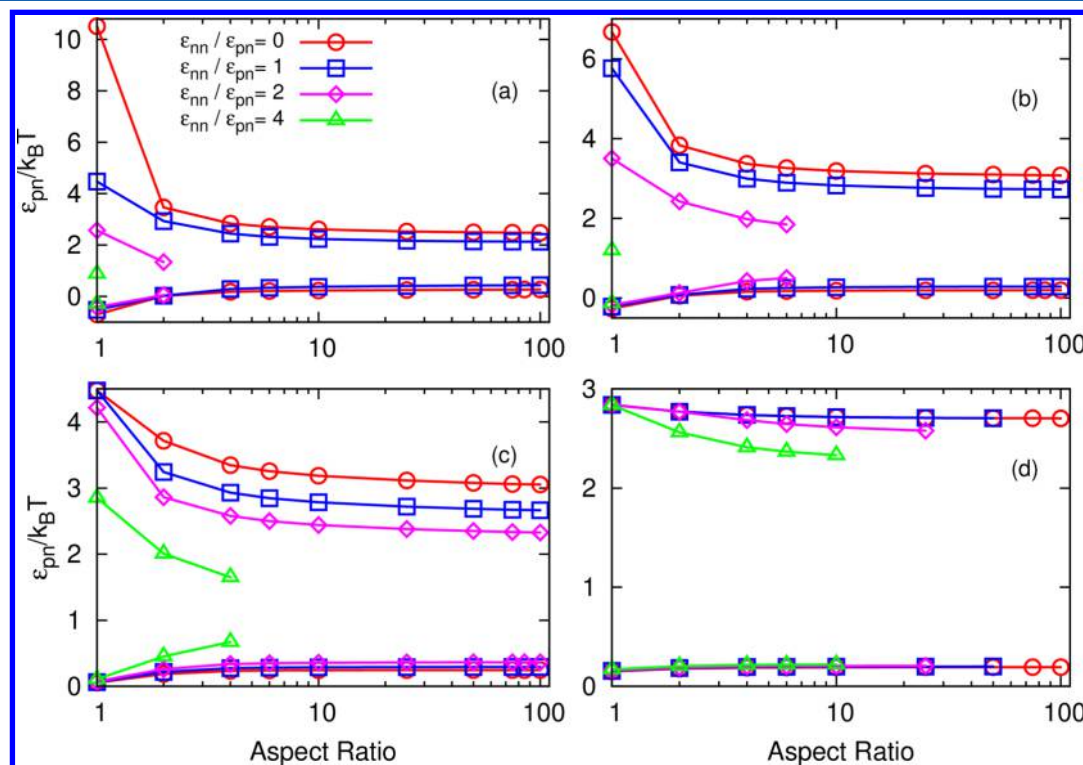
Figure 6. Spinodal phase diagrams of polymer-nanorod composites in the polymer−particle attraction strength (ε_{pn}/k_BT) − aspect ratio plane at different $\varepsilon_{nn}/\varepsilon_{pn}$. AR = 1 refers to nanospheres, noninteracting ($\varepsilon_{nn}/\varepsilon_{pn}$ = 0) nanorods are represented by red circles, $\varepsilon_{nn}/\varepsilon_{pn}$ = 1 are given by blue squares, $\varepsilon_{nn}/\varepsilon_{pn}$ = 2 are given by pink diamonds, and $\varepsilon_{nn}/\varepsilon_{pn}$ = 4 are represented by green triangles. The four panels represent different ratios of nanorod to monomer diameters (a) D/d = 1, (b) D/d = 2, (c) D/d = 4, and (d) D/d = 10.

have found that when the HNC closure is used for polymer−particle interactions, the depletion boundary either changes nonmonotonically, or falls with aspect ratio especially for larger diameter nanorods (not shown). This contradicts simulation results[63] and provides additional justification for the closure scheme well established in the literature.[26,44,62] Figures 6a, and 6b indicate that the depletion-driven spinodal boundary for the smaller nanospheres ($D/d = 1$ and $D/d = 2$) lies below $\varepsilon_{pn} = 0$; i.e., these particles are miscible in the polymer melt even in the absence of attractive interactions. In fact, the appearance of the spinodal boundary at $\varepsilon_{pn} < 0$ indicates that polymer−particle repulsions are required to drive phase separation. In both cases, the polymer radius of gyration is significantly larger than the size of the nanosphere ($Rg_{poly}/D \sim 5.43$ for $D/d = 1$, and $Rg_{poly}/D \sim 2.71$ for $D/d = 2$). At $D/d = 4$, the particle diameter approaches the radius of gyration of the polymer ($Rg_{poly}/D \sim 1.36$), and the spinodal boundary is predicted slightly above $\varepsilon_{pn} = 0$. This is in agreement with experiments of Mackay et al.,[24] which suggest that the boundary of miscibility between chemically similar polymer-nanosphere mixtures lies at $Rg_{poly} \sim D$. Figure 6 demonstrates that the miscibility window narrows rapidly for small aspect ratio nanorod composites, while for larger aspect ratios, both the depletion and bridging curves become nearly independent of rod aspect ratio. The miscibility limits also vary more quickly at smaller nanorod diameters. These two effects are studied together in Figure 7.
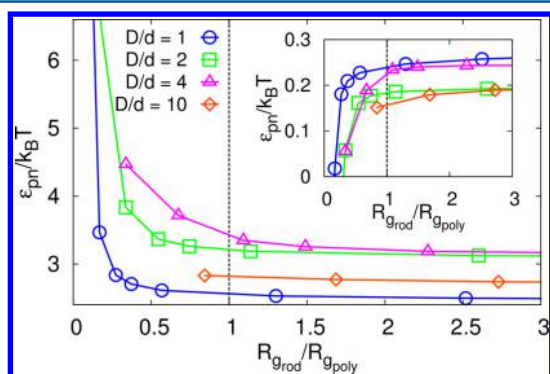
Figure 7. Main panel presents the spinodal boundary in the bridging region as a function of the ratio of nanorod radius of gyration to polymer radius of gyration (R_{rod}/Rg_{poly}) at $\varepsilon_{nn}/\varepsilon_{pn} = 0$, and the inset illustrates the spinodal in the depletion region at various D/d. Here, $D/d = 1$ systems are given by blue circles, $D/d = 2$ by green squares, $D/d = 4$ by pink triangles, and $D/d = 10$ by orange diamonds. The dashed vertical lines are drawn at $Rg_{rod}/Rg_{poly} = 1$ for emphasis.

The main panel of Figure 7 presents the spinodal boundaries of athermally interacting rods ($\varepsilon_{nn}/\varepsilon_{pn} = 0$) in the bridging regime as a function of the ratio of the nanorod radius of gyration (Rg_{rod}) to the polymer radius of gyration (Rg_{poly}), while the inset presents the data in the depletion regime. The rod radius of gyration is described by,

$$Rg_{rod} = \frac{\sqrt{\sum_{\nu,\gamma=1}^{N_n} (\vec{r_\nu} - \vec{r_\gamma})^2}}{\sqrt{2}\,N_n} + \frac{D}{2} \qquad (12)$$

where, N_n is the number of spherical sites in a rod, while r_ν and r_γ are the position of these sites. Rg_{god} is a function of both the aspect ratio, and the diameter of the rod. Figure 7 shows that the boundaries of phase separation change quickly in both regimes when $Rg_{rod} < Rg_{poly}$, and are nearly constant for $Rg_{rod}/Rg_{poly} > 1$. It is therefore clear that the miscibility window is a sensitive function of the nanorod size while it is smaller than the polymer radius of gyration, and is nearly independent of rod-length beyond this limit. Most free volume theories,[15−17] scaling theories,[71,72] integral equation theories,[26] simulations,[71,73] and experiments[24] have studied the effect of nano*sphere* diameter on the depletion−attraction, and have found monotonic behavior. However, it is apparent from Figures 6 and 7 that the spinodal boundaries, as they approach their "asymptotic values" at both low and high ε_{pn}, are a nonmonotonic function of the nano*rod* diameter.

According to the coarse-grained Asakura−Oosawa (AO) depletion potential between nanospheres,[15] which has been found to be applicable for $Rg_{poly} < D$,[74] both the strength and the range of the depletion-attraction increase with particle size. (It is worth noting that at $Rg_{poly}/D \sim 0.23$, experiments[74] and simulations[75] making use of the AO potential demonstrate the appearance of a crystalline phase.) Scaling theory[71,72] and computer simulations[73,76] have demonstrated that the attraction strength of the depletion potential when $Rg_{poly} > D$, is proportional to the nanosphere diameter. While these theories and simulations are applicable in the dilute to semidilute polymer regime, experiments[24] in the melt regime have demonstrated depletion driven phase separation to be prominent when $Rg_{poly} < D$. A functional form of the entropy-driven depletion-attraction has not yet been well established for the melt regime. The dependence of the spinodal boundary on nanosphere and nanorod diameters (at $\varepsilon_{nn}/\varepsilon_{pn} = 0$) is shown in Figure 8. Figure 8a illustrates that the depletion boundary rises as a function of the nanosphere diameter suggesting that the depletion−attraction in melts also increases with particle size. Meanwhile, the bridging curve falls monotonically, resulting in the consistent narrowing of the miscibility region as a function of nanosphere size. The variability in the two phase-boundaries decreases with increasing size, and the width of the homogeneous region becomes nearly constant for large nanospheres.

While it is understood that depletion-induced effective attractions between particles are an increasing function of the size of the nanoparticle (at least in the dilute and semidilute regimes), the reason for the ease in bridging-induced phase separation with increasing nanosphere diameter is not immediately clear. It is possible that the availability of large contiguous nanoparticle surfaces for polymer adsorption drives bridging-induced phase separation for larger nanospheres. This may also be the reason for the fall in the bridging curves with increasing aspect ratio (as demonstrated by Figure 6). However, Figure 8b shows that neither the depletion, nor the bridging boundaries are monotonically dependent on nanorod (aspect ratio=10) diameter. The depletion boundary displays a minimum at $D/d = 2$ and a maximum at $D/d = 4$, while the bridging boundary displays a maximum at $D/d = 6$ (when $Rg_{poly} \sim D$). The miscibility window, as a result, first widens and then narrows as a function of nanorod diameter. An important difference between spheres and rods is that while spheres are modeled as perfectly smooth objects, the rods have surface roughness imposed by their composition as tangentially arranged spherical sites. In order to check if this nonmonotonic behavior is due to surface corrugations imposed on the rods due to our site-level description, we have calculated the phase boundaries for a rod of AR = 10 described by a set of overlapping spheres, with $L/D = 0.5$. In this case, the rod surface is much smoother. Figure 8b presents a schematic of
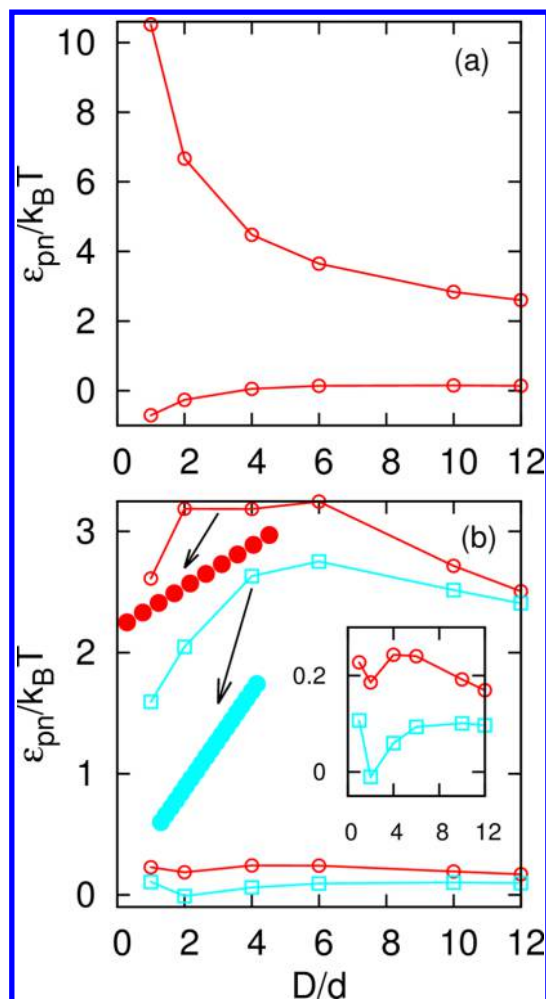
Figure 8. (a) Spinodal phase diagram of polymer-nanosphere systems as a function of the ratio of nanosphere to monomer diameter, at $\varepsilon_{nn}/\varepsilon_{pn} = 0$. (b) Spinodal diagram of polymer-nanorod systems at AR = 10 and $\varepsilon_{nn}/\varepsilon_{pn} = 0$. The red circles represent rough rods with $L/D = 1$, and the blue squares represent the smoother rods with $L/D = 0.5$. The arrows point to schematics of the rods. The inset is a magnified representation of data in the depletion region.

both kinds of rods as well as their phase boundaries as a function of D/d. For the smoother rods, the spinodal curve corresponding to both depletion and bridging fall to lower values of ε_{pn}. The spinodal in the depletion regime displays a deeper minimum at $D/d = 2$, while the maximum at $D/d = 4$ vanishes. The bridging boundary displays a more positive slope for $D/d < 6$ and a less negative slope for $D/d > 6$. However, the nonmonotonic behavior of the spinodal in the bridging regime persists for these smoother nanorod composites. It is possible that the negative slope of the bridging boundary for $D/d > 6$ may become zero or positive for infinitely smooth rods, resulting in a monotonically rising bridging boundary as the rod thickness increases (or curvature decreases). However, our current calculations do not put us in a position to comment on this matter. Hence, it seems that while the bridging boundary falls and the depletion line rises monotonically as a function of nanosphere diameter, rod diameters have a subtle and nonmonotonic effect on miscibility in both the bridging and the depletion regimes.

The solvent-mediated average force between colloidal particles have been of interest both in terms of understanding the physics of composite systems and in developing coarse graining methods for mesoscale simulations. Figure 9 illustrates the (orientationally averaged) polymer-mediated forces between rods, as calculated by eq 10. The forces are determined close to the depletion (Figure 9, parts a and b) and bridging (Figure 9, parts c and d) spinodal boundaries and divided by the particle diameter, D. Figure 9a presents the large depletion-induced attractive force that brings rods into contact. It shows that polymer-mediated inter-rod forces, at and beyond contact, are proportional to the nanorod diameter. Similar behavior has been previously predicted in the dilute nanosphere limit,[26] and here we show that the scaling of the interparticle forces ($f_{nn} \propto D$) can be generalized to the rod-like nanoparticles. In fact, Figure 9b, which plots the force between two nanorods at fixed $D/d = 4$, and various aspect ratios demonstrates that the force is independent of rod length. Small fluctuations in the force curve that appear in Figure 9, parts a and b, at length-scales equivalent to the rod diameter arise from the cusps in the radial distribution function signaling the existence of neighboring sites in a rod. These fluctuations are a result of the spherical-site level description of a nanorod, and hence can be ignored for smooth rods. Figure 9c presents the force curves of AR = 10 rods at various D/d close to bridging-driven phase separation. While it shows that the location of the attractive minimum now appears at $r = D + d$, where bridging takes place, it also demonstrates roughly the same $f_{nn} \propto D$ scaling behavior is exhibited close to the bridging boundary. Simulations have also predicted that the minimum in the bridging force increases with spherical particle diameter.[33] Here, we show that the dependence is approximately linear. Finally, Figure 9d shows that the inter-rod forces are also independent of aspect ratio in the bridging regime (as is the case in the depletion regime).

C. Attractive Rods. Along with the spinodal boundaries of hard-core interacting rods, Figure 6 also presents the phase diagram of attractive rods with $\varepsilon_{nn}/\varepsilon_{pn} = 1$, 2, and 4. It is clear that with increasing rod−rod attraction strength, the depletion boundary rises and the spinodal boundary at high ε_{pn} falls, resulting in the rapid narrowing of the miscibility window, particularly for long and thin rods. At $\varepsilon_{nn}/\varepsilon_{pn} = 2$ and 4, this narrow miscibility window makes it difficult to reach a convergent solution to the integral equations. As a result, only the phase boundaries at low aspect ratios have been determined. Carbon nanotubes have aspect ratios on the order of $\sim 10^2 - 10^3$, and intertube attractions on the order of $\sim 10 k_B T$. Therefore, the narrowing of the miscible regime with both increasing $\varepsilon_{nn}/\varepsilon_{pn}$ and aspect ratio indicate that it is not possible to stabilize unmodified carbon nanotube-polymer composites. Figure 10a plots the radial distribution function of rods with an aspect ratio of 4, and $D/d = 4$ near the high-ε_{pn} spinodal. It shows that while at $\varepsilon_{nn}/\varepsilon_{pn} = 0,1$ and 2 the prominent peak is the bridging peak at $r = D + d$, at $\varepsilon_{nn}/\varepsilon_{pn} = 4$ the largest peak shifts to $r = D$ (i.e., contact). Hence, the bridged structures give way to contact-dominant clusters, and the macrophase separation changes from a bridging-driven to a contact-driven phase separation, at such large inter-rod attractions. In this regime, the clustering behavior is dominated by structures such as those illustrated by Figure 3a, while a few arrangements of the kind depicted in Figure 3b are also present. Figure 10b presents the radial distribution functions for $D/d = 10$ rods (aspect ratio = 4) near the bridging spinodal at various $\varepsilon_{nn}/\varepsilon_{pn}$. As the inter-rod attractions increase so do the peak heights. Here, it is clear that the telebridging behavior persists even at $\varepsilon_{nn}/\varepsilon_{pn} = 4$, and does not give way to a contact dominated
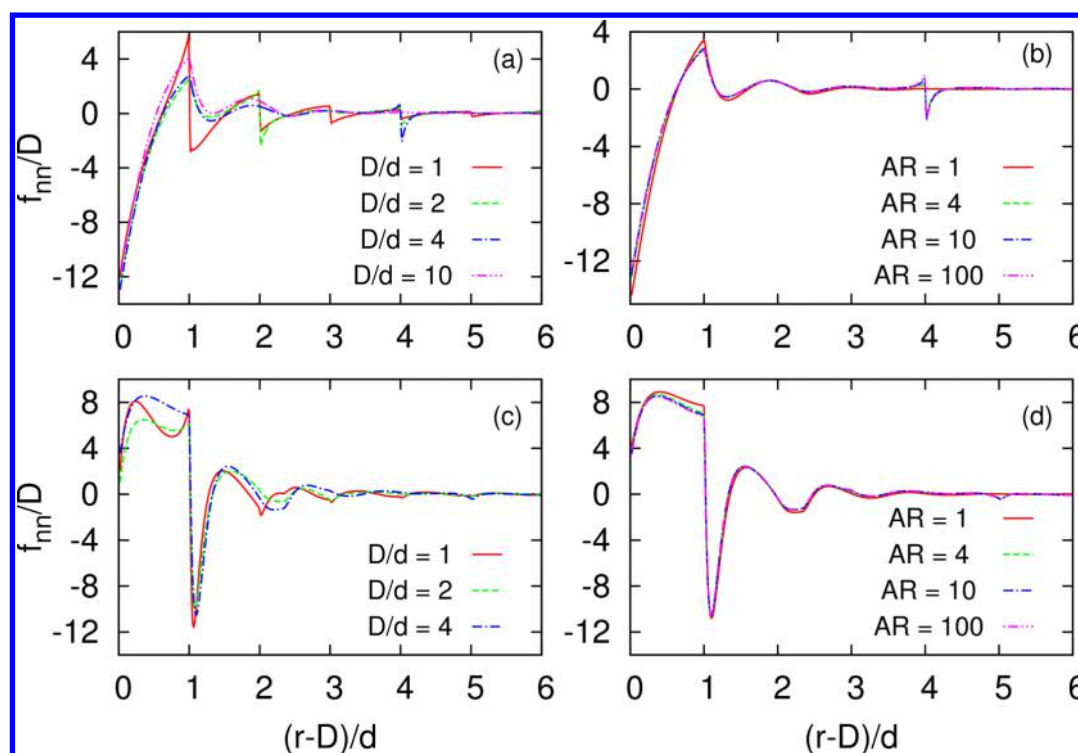
Figure 9. Polymer-mediated inter-rod forces normalized by rod diameter (f_{nn}/D) as a function of $(r - D)/d$ at $\varepsilon_{nn}/\varepsilon_{pn} = 0$ and various aspect ratios and rod diameters. (a) AR = 10 rods close to the depletion boundary ($\varepsilon_{pn} = 0.3k_BT$) at various D/d: $D/d = 1$ (solid, red line), $D/d = 2$ (dashed, green line), $D/d = 4$ (dot-dashed, blue line), and $D/d = 10$ (dot-dot-dashed, pink line). (b) $D/d = 4$ rods close to the depletion boundary ($\varepsilon_{pn} = 0.3k_BT$) at various aspect ratios: AR = 1 (solid, red line), AR = 4 (dashed, green line), AR = 10 (dot-dashed, blue line), and AR = 100(dot-dot-dashed pink line). (c) AR = 10 rods close to the bridging boundary ($\varepsilon_{pn} = 2.5k_BT$) at various D/d: $D/d = 1$ (solid, red line), $D/d = 2$ (dashed, green line), $D/d = 4$ (dot-dashed, blue line). (d) $D/d = 4$ rods close to the bridging boundary ($\varepsilon_{pn} = 2.5k_BT$) at various aspect ratios: AR = 1 (solid, red line), AR = 4 (dashed, green line), AR = 10 (dot-dashed, blue line), and AR = 100 (dot-dot-dashed pink line).

phase separation. However, largest peak gradually shifts from $r = D + 3d$ to $r = D + 2d$, indicating that the particles prefer to be bridged by two bound polymer layers rather than three bound polymer layers as attractions increase.

The preference for contact dominated versus bridging dominated phase separation at the high-ε_{pn} boundary is presented by Figure 11. It plots the contact (filled symbols) and bridging (open symbols) values of the rod−rod radial distribution function against rod aspect ratio for several rod diameters at $\varepsilon_{nn}/\varepsilon_{pn} = 1$ (Figure 11a) and $\varepsilon_{nn}/\varepsilon_{pn} = 2$ (Figure 11b). Figure 11a shows that at $\varepsilon_{nn}/\varepsilon_{pn} = 1$, spheres and rods prefer contact-driven phase separation for $D/d = 1$ and bridging driven phase separation at $D/d = 4$ irrespective of aspect ratio. At $D/d = 2$, it is predicted that while nanospheres prefer contact aggregation, and nanorods show bridging dominated phase reparation. As would be expected, at higher $\varepsilon_{nn}/\varepsilon_{pn} = 2$ (Figure 11b) the behavior shifts more toward contact aggregation. Here, rods of all available aspect ratios undergo contact driven phase separation at $D/d = 1$, and 2, while they undergo bridging induced phase separation at $D/d = 4$. At $D/d = 10$, telebridging is predicted for all aspect ratios and at all $\varepsilon_{nn}/\varepsilon_{pn}$ (data not shown), while telebridging gradually changes to fewer number of bound polymer layers as $\varepsilon_{nn}/\varepsilon_{pn}$ increases. As discussed earlier, an example of this behavior is reflected in Figure 10b. Hence, rods of larger diameters and longer aspect ratios prefer bridging aggregation to contact aggregation. It is possible to envision a situation where longer inter-rod attractive ranges, would allow rods to experience attractions even while bridged by a polymer layer. Since the range of attraction

between rods scales with rod diameter, it is worthwhile to ask whether the predominance of bridging correlations at large particle diameters is actually related to an increase in the range of attraction. To check whether the crossover from contact to bridging, as the rod diameter increases, is a result of longer rod−rod attraction range we have calculated the radial distribution functions for larger diameter ($D/d = 4$) rods at various ranges of attraction, and have found that the thicker rods prefer bridging driven phase separation irrespective of attraction range (see Supporting Information). Hence the contact to bridging crossover is not a function of the attractive range but an independent function of the rod diameter.

IV. CONCLUSIONS

We find that nanoparticles are miscible in a polymer melt in the presence of moderate attractions between polymer and nanoparticle. As has been predicted by others,[27,28,30,31,44] nonadsorbing polymers undergo depletion driven phase separation from nanospheres (given that the nanosphere size is on the order of, or larger than, the radius of gyration of the polymer), and highly adsorbing polymers give rise to a bridging driven aggregation. We find that the same behavior applies to nanorods. When the range of this attraction is long, telebridging behavior is predicted for nanorods of all aspect ratios. Telebridging occurs because longer polymer−particle attraction ranges allow nanoparticles to be bridged by multiple polymer layers since these configurations allow several polymers to simultaneously experience attractions with the bridged nano-particles. The attractive range, in this case, is required to be
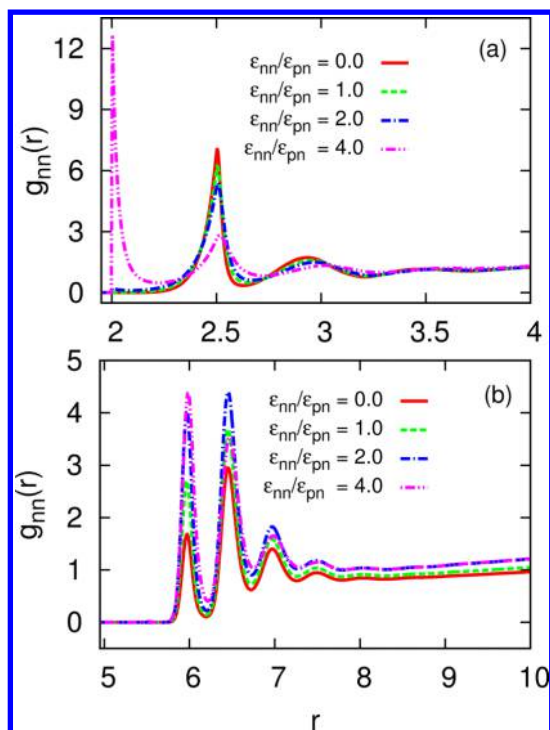
Figure 10. Particle–particle radial distribution function at the high ε_{pn} boundary for nanorods with AR = 4 and different $\varepsilon_{nn}/\varepsilon_{pn}$: $\varepsilon_{nn}/\varepsilon_{pn} = 0$ (solid, red line), $\varepsilon_{nn}/\varepsilon_{pn} = 1$ (dashed, green line), $\varepsilon_{nn}/\varepsilon_{pn} = 2$ (dot-dashed blue line), and $\varepsilon_{nn}/\varepsilon_{pn} = 4$ (dot-dot-dashed pink line). (a) $D/d = 4$ rods. (b) $D/d = 10$ rods.
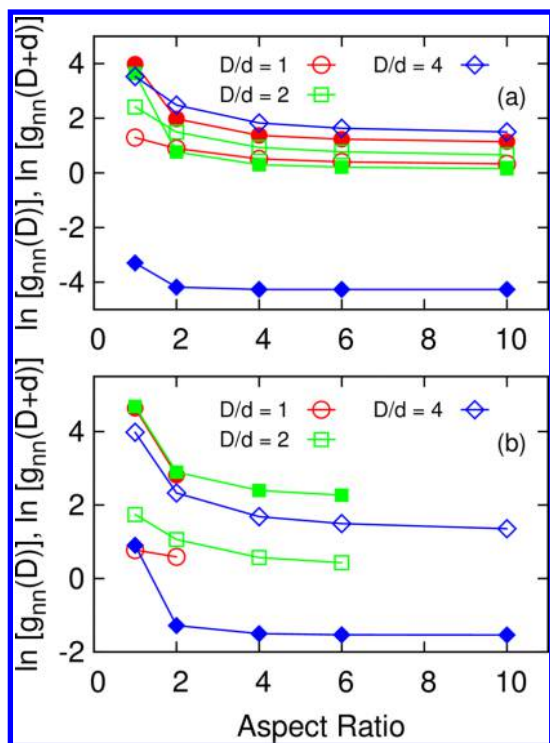
Figure 11. Natural logarithm of the value of particle–particle radial distribution function at contact, $\ln(g_{nn}(D))$, and at bridging, $\ln(g_{nn}(D + d))$, as a function of aspect ratio at various D/d: $D/d = 1$ (red circles), $D/d = 2$ (green squares), and $D/d = 4$ (blue diamonds). Filled symbols represent contact value and open symbols represent bridging values. (a) $\varepsilon_{nn}/\varepsilon_{pn} = 1$. (b) $\varepsilon_{nn}/\varepsilon_{pn} = 2$.

large in comparison to the monomer diameter, rather than the nanoparticle diameter. Our calculations for athermally interacting nanospheres qualitatively agree with experiments demonstrating miscibility for chemically similar polymer and nanoparticles when the particles are smaller than the polymer radius of gyration, and immiscibility when larger particles are chosen.[24] The rising spinodal boundary (as a function of aspect ratio) in the depletion regime, also agrees with recent dissipative dynamics simulations which demonstrate decreasing miscibility of nanorods as a function of aspect ratio.[63] Furthermore, we predict that for long aspect ratios, the spinodal boundary occurs at nearly constant values of the polymer adsorption strength. The bridging spinodal boundary is observed first to fall quickly and then remain nearly constant as a function of rod length. This leads to a fast narrowing of the miscibility window, followed by a nearly fixed width. There is a crossover in the behavior of the spinodal boundaries, in both the depletion and bridging regimes, from quickly varying to remaining nearly constant. We have demonstrated that this crossover occurs when the rod radius of gyration exceeds the polymer radius of gyration.

Interestingly, we find that while both the bridging and depletion boundaries of nanosphere-polymer mixtures vary monotonically with nanosphere diameter, these boundaries are a subtle nonmonotonic function of nanorod thickness. In the case of polymer nanosphere composites, the location of the bridging boundary falls, and the depletion boundary rises, in terms the polymer–particle attraction strength, yielding a steadily narrowing miscible region as a function of nanoparticle size. The miscibility window of nanorod composites first widens and then narrows as a function of rod diameter. We have examined the role of nanorod surface roughness on the stability of the composite and have found this to be a significant factor. The location of both bridging and depletion boundaries fall for smoother nanorods. The polymer mediated inter-rod forces both at contact (in the depletion regime) and at bridging distances (in the bridging regime) are found to be proportional to the nanorod diameter, and independent of aspect ratio.

The miscible region rapidly narrows as the attraction between the nanorods increases, particularly for thin nanorods (*thin*, compared to the monomer diameter). This suggests that it is not possible to form thermodynamically stable unmodified single walled carbon nanotube–polymer composites. At high polymer adsorption strengths, bridging correlations are supplanted by direct nanorod contacts, and telebridged structures incur a reduction in the number of adsorbed polymer layers. The change from bridging dominated to contact dominated structures occurs more quickly for short and thin rods, as the inter-rod attractions increase.

■ ASSOCIATED CONTENT

Ⓢ Supporting Information

Data which show that the increasing tendency of thicker attractive rods to form bridged (rather than contact dominated) structures at the high ε_{pn} boundary is independent of the range of rod–rod attractions. This material is available free of charge via the Internet at http://pubs.acs.org.

■ AUTHOR INFORMATION

Corresponding Author

*(M.T.) E-mail: tripathy@iitb.ac.in.

REFERENCES

(1) Kumar, S. K.; Krishnamoorti, R. *Annu. Rev. Chem. Biomol. Eng.* **2010**, *1*, 37−58.
(2) Paul, D. R.; Robeson, L. M. *Polymer* **2008**, *49*, 3187−3204.
(3) Moniruzzaman, M.; Winey, K. I. *Macromolecules* **2006**, *39*, 5194−5205.
(4) Deluca, N. W.; Elabd, Y. A. *J. Polym. Sci., Part B: Polym. Phys.* **2006**, *44*, 2201−2225.
(5) Kongkanand, A.; Kuwabata, S.; Girishkumar, G.; Kamat, P. *Langmuir* **2006**, *22*, 2392−2396.
(6) Villmow, T.; Pegel, S.; John, A.; Rentenberger, R.; Pötschke, P. *Mater. Today* **2011**, *14*, 340−345.
(7) Villmow, T.; John, A.; Pötschke, P.; Heinrich, G. *Polymer* **2012**, *53*, 2908−2918.
(8) Kim, H.-W.; Kim, H.-E.; Salih, V. *Biomaterials* **2005**, *26*, 5221−5230.
(9) Hule, R. A.; Pochan, D. J. *MRS Bull.* **2007**, *32*, 354−358.
(10) Toprak, M. S.; Mckenna, B. J.; Waite, J. H.; Stucky, G. D. *Chem. Mater.* **2007**, *19*, 4263−4269.
(11) Bryning, B. M. B.; Islam, M. F.; Kikkawa, J. M.; Yodh, A. G. *Adv. Mater.* **2005**, *17*, 1186−1191.
(12) White, S. I.; Mutiso, R. M.; Vora, P. M.; Jahnke, D.; Hsu, S.; Kikkawa, J. M.; Li, J.; Fischer, J. E.; Winey, K. I. *Adv. Funct. Mater.* **2010**, *20*, 2709−2716.
(13) Wang, D.; Hore, M. J. a; Ye, X.; Zheng, C.; Murray, C. B.; Composto, R. J. *Soft Matter* **2014**, *10*, 3404−3413.
(14) Huynh, W. U.; Dittmer, J. J.; Alivisatos, A. P. *Science* **2002**, *295*, 2425−2427.
(15) Asakura, S.; Oosawa, F. *J. Polym. Sci.* **1958**, *33*, 183−192.
(16) Asakura, S.; Oosawa, F. *J. Chem. Phys.* **1954**, *22*, 1255.
(17) Gast, A. P.; Hall, C. K.; Russel, W. B. *J. Colloid Interface Sci.* **1983**, *96*, 251−267.
(18) Vrij, A. *Pure Appl. Chem.* **1976**, *48*, 471−483.
(19) Haggenmueller, R.; Zhou, W.; Fischer, J. E.; Winey, K. I. *J. Nanosci. Nanotechnol.* **2003**, *3*, 105−110.
(20) Ramasubramaniam, R.; Chen, J.; Liu, H. *Appl. Phys. Lett.* **2003**, *83*, 2928−2930.
(21) Kashiwagi, T.; Du, F.; Douglas, J. F.; Winey, K. I.; Harris, R. H.; Shields, J. R. *Nat. Mater.* **2005**, *4*, 928−933.
(22) Du, F.; Fischer, J. E.; Winey, K. I. *J. Polym. Sci., Part B: Polym. Phys.* **2003**, *41*, 3333−3338.
(23) Bandyopadhyaya, R.; Nativ-roth, E.; Regev, O.; Yerushalmi-rozen, R. *Nano Lett.* **2002**, *2*, 25−28.
(24) Mackay, M. E.; Tuteja, A.; Duxbury, P. M.; Hawker, C. J.; Van Horn, B.; Guan, Z.; Chen, G.; Krishnan, R. S. *Science* **2006**, *311*, 1740−1743.
(25) Smith, J. S.; Bedrov, D.; Smith, G. D. *Compos. Sci. Technol.* **2003**, *63*, 1599−1605.
(26) Hooper, J. B.; Schweizer, K. S.; Desai, T. G.; Koshy, R.; Keblinski, P. *J. Chem. Phys.* **2004**, *121*, 6986−6997.
(27) Hooper, J. B.; Schweizer, K. S. *Macromolecules* **2005**, *38*, 8858−8869.
(28) Hooper, J. B.; Schweizer, K. S. *Macromolecules* **2006**, *39*, 5133−5142.
(29) Zhao, L.; Li, Y.; Zhong, C. *J. Chem. Phys.* **2007**, *126*, 014906.
(30) Liu, J.; Gao, Y.; Cao, D.; Zhang, L.; Guo, Z. *Langmuir* **2011**, *27*, 7926−7933.
(31) Patra, T. K.; Singh, J. K. *J. Chem. Phys.* **2013**, *138*, 144901.
(32) Patra, T. K.; Singh, J. K. *Soft Matter* **2014**, *10*, 1823−1830.
(33) Marla, K. T.; Meredith, J. C. *Langmuir* **2005**, *21*, 487−497.
(34) Huang, J.; Mao, Z.; Qian, C. *Polymer* **2006**, *47*, 2928−2932.
(35) Zhang, Q.; Archer, L. A. *J. Chem. Phys.* **2004**, *121*, 10814.
(36) Lekkerkerker, H. N. W.; Stroobants, A. *Nuovo Cim.* **1994**, *16*, 949−962.
(37) Savenko, S. V.; Dijkstra, M. *J. Chem. Phys.* **2006**, *124*, 234902.
(38) Karatrantos, A.; Composto, R. J.; Winey, K. I.; Clarke, N. *Macromolecules* **2011**, *44*, 9830−9838.
(39) Ganesan, V.; Khounlavong, L.; Pryamitsyn, V. *Phys. Rev. E* **2008**, *78*, 051804.
(40) Frischknecht, A. L.; McGarrity, E. S.; Mackay, M. E. *J. Chem. Phys.* **2010**, *132*, 234902.
(41) Surve, M.; Pryamitsyn, V.; Ganesan, V. *Macromolecules* **2007**, *40*, 344−354.
(42) Frischknecht, A. L. *J. Chem. Phys.* **2008**, *128*, 224902.
(43) Frischknecht, A. L.; Hore, M. J. A.; Ford, J.; Composto, R. J. *Macromolecules* **2013**, *46*, 2856−2869.
(44) Hall, L. M.; Schweizer, K. S. *Soft Matter* **2010**, *6*, 1015.
(45) Hore, M. J. A.; Frischknecht, A. L.; Composto, R. J. *ACS Macro Lett.* **2012**, *1*, 115−121.
(46) Du, F.; Scogna, R. C.; Zhou, W.; Brand, S.; Fischer, J. E.; Winey, K. I. *Macromolecules* **2004**, 9048−9055.
(47) Sumfleth, J.; Buschhorn, S. T.; Schulte, K. *J. Mater. Sci.* **2011**, *46*, 659−669.
(48) Penu, C.; Hu, G.; Fernandez, A.; Marchal, P.; Choplin, L. *Polym. Eng. Sci.* **2012**, *52*, 2173−2181.
(49) Kota, A. K.; Cipriano, B. H.; Duesterberg, M. K.; Gershon, A. L.; Powell, D.; Raghavan, S. R.; Bruck, H. A. *Macromolecules* **2007**, *40*, 7400−7406.
(50) Leung, K.; Chandler, D. *J. Stat. Phys.* **1991**, *63*, 837−856.
(51) Kyrylyuk, A. V.; van der Schoot, P. *Proc. Natl. Acad. Sci. U.S.A.* **2008**, *105*, 8221−8226.
(52) Otten, R. H. J.; van der Schoot, P. *Phys. Rev. Lett.* **2009**, *103*, 225704.
(53) Jadrich, R.; Schweizer, K. S. *J. Chem. Phys.* **2011**, *135*, 234902.
(54) Chatterjee, A. P. *J. Stat. Phys.* **2012**, *146*, 244−248.
(55) Chatterjee, A. P. *J. Chem. Phys.* **2010**, *132*, 224905.
(56) Philipse, A. P. *Langmuir* **1996**, *12*, 1127−1133.
(57) Chatterjee, A. P. *J. Phys.: Condens. Matter* **2008**, *20*, 255250.
(58) Foygel, M.; Morris, R.; Anez, D.; French, S.; Sobolev, V. *Phys. Rev. B* **2005**, *71*, 104201.
(59) Nigro, B.; Grimaldi, C.; Ryser, P.; Chatterjee, A. P.; van der Schoot, P. *Phys. Rev. Lett.* **2013**, *110*, 015701.
(60) Wang, X.; Chatterjee, A. P. *J. Chem. Phys.* **2004**, *118*, 10787.
(61) Sen, S.; Xie, Y.; Kumar, S. K.; Yang, H.; Ho, D. L.; Hall, L.; Hooper, J. B.; Schweizer, K. S. *Phys. Rev. Lett.* **2007**, *98*, 128302.
(62) Hall, L. M.; Anderson, B. J.; Zukoski, C. F.; Schweizer, K. S. *Macromolecules* **2009**, *42*, 8435−8442.
(63) Hu, S.-W.; Sheng, Y.-J.; Tsao, H.-K. *Soft Matter* **2013**, *9*, 7261−7266.
(64) Chandler, D. *J. Chem. Phys.* **1972**, *57*, 1930.
(65) Schweizer, K. S.; Curro, J. G. *Macromolecules* **1988**, *21*, 3070−3081.
(66) Schweizer, K. S.; Curro, J. G. *Macromolecules* **1988**, *21*, 3082−3087.
(67) Schweizer, K. S.; Curro, J. G. *Adv. Chem. Phys.* **1997**, *98*, 1−142.
(68) Henderson, D.; Duh, D.-M.; Chu, X.; Wasan, D. *J. Colloid Interface Sci.* **1997**, *185*, 265−268.
(69) Hall, L. M.; Schweizer, K. S. *J. Chem. Phys.* **2008**, *128*, 234901.
(70) Sen, S.; Thomin, J. D.; Kumar, S. K.; Keblinski, P. *Macromolecules* **2007**, *40*, 4059−4067.
(71) Louis, A. A.; Bolhuis, P. G.; Meijer, E. J.; Hansen, J. P. *J. Chem. Phys.* **2002**, *117*, 1893−1907.
(72) Joanny, J. F.; Leibler, L.; de Gennes, P.-G. *J. Polym. Sci. Part B* **1979**, *17*, 1073−1084.
(73) Bolhuis, P. G.; Meijer, E. J.; Louis, A. A. *Phys. Rev. Lett.* **2003**, *90*, 068304.
(74) Ilett, S. M.; Orrock, A.; Poon, W. C. K.; Pusey, P. N. *Phys. Rev. E* **1995**, *51*, 1344−1353.

(75) Meijer, E. J.; Frenkel, D. *J. Chem. Phys.* **1994**, *100*, 6873−6887.
(76) Cao, X.-Z.; Merlitz, H.; Wu, C.-X.; Sommer, J.-U. *Phys. Rev. E*
2011, *84*, 041802.